Composite Structures 206 (2018) 234–246

Contents lists available at ScienceDirect

Composite Structures

journal homepage: www.elsevier.com/locate/compstruct

A supervised iterative approach to 3D microstructure reconstruction from acquired tomographic data of heterogeneous fibrous systems

Ronald F. Agyei, Michael D. Sangid*

School of Aeronautics and Astronautics, Purdue University, 701 W Stadium Ave, West Lafayette, IN, USA

ARTICLE INFO

Keywords:
Discontinuous reinforcement
Glass fibers
Non-destructive testing
Radiography
Injection molding

ABSTRACT

The recent ubiquitous utilization of short fiber reinforced composites (SFRCs) in applications that require complex shape conforming, light-weight materials with good strength properties, calls for in-depth studies to understand the underpinning physics behind SFRCs response to load and consequently damage. Since the accuracy of such studies is contingent on successful sub-volume characterization, the intricate sub-volume architecture of SFRCs requires conscientious methodology that addresses complex morphologies like fiber cross-overs, which is by no means a trivial endeavor. This paper proposes a novel framework that hinges on the synergy between robust 2D segmentation and 3D volume reconstruction techniques to faithfully reconstruct the fiber architecture of 3D X-ray tomograms of SFRCs. The implications of this framework not only include a platform that fully characterizes the complex sub-volume, but also provides a convenient means of incorporating tracking algorithms necessary for the in-situ characterization of the reconstructed fibers, if desired.

1. Introduction

Short fiber reinforced composites (SFRCs), though less stiff than continuous reinforced composites, are largely used for applications which require lightweight materials with good mechanical properties as well as have the ability to form complex shapes at minimal cost [1,2] usually achieved by injection molding [3–5]. The mechanical behavior of SFRCs is dictated by its fiber orientation and length distributions, mean free paths, the presence of voids and microcracks, to name but a few [6–10]. Therefore in order to elucidate the constitutive response to load and consequently failure, reliable frameworks are required to effectively characterize SFRCs.

Early attempts at microstructure characterization of SFRCs comprised destructive 2D characterization techniques which include image analysis of consecutive polished surfaces through microscopy in its varying forms [11]. However, not only are these techniques susceptible to erroneous results arising from non-parallel 2D sectioning, fiber morphology distortion during handling, etc., but also the permanent deterioration of the specimen makes destructive 2D characterization approaches unsuitable for in-situ characterization [12–14]. The recent emergence of non-destructive testing, on the other hand, affords precision in the probing of SFRCs at extremely minute length scales, usually on the order of microns, without altering their original constituents [15–20]. This paper presents a novel non-destructive framework using a combination of radiography and sub-volume reconstruction techniques to probe the complex microstructures of fibrous systems, employing SFRCs as a case study.

In the use of radiography for microstructural analysis, it is commonplace to reconstruct the fibrous systems from a set of grayscale 2D image slices acquired from radiography (3D image volumes) and this has led to several proposed frameworks dedicated to efficient 3D sub-volume reconstruction. Some frameworks, a few of which will be discussed, rely directly on the fiber intensity maps on grey level image volumes to perform 3D fiber reconstruction. Eberhard and Clarke [21] proposed an automated 3D fiber reconstruction framework where the building blocks were a set of vectors traced in directions of highest mean pixel intensity (most probable fiber orientation). Neighboring vectors aligned in similar orientations were connected in a chain and subsequently curved fit to represent fiber centerlines. It is important to note that this method of fiber tracing could be compromised when adopted in noisy images or image volumes of highly clustered fibers characterized by high incidence of fiber cross-overs. Sandau and Osher [22] address the crossing fiber segmentation problem by proposing a framework that adopts a locally adaptive threshold using the so-called chord length transform to identify crossing points, however, it is still difficult to identify which fibers are separated and which ones are secondary branches [23]. The framework of Viguié et al. [24] analyzes the subtle variations of the local fiber orientation to identify fibers with

* Corresponding author.
E-mail address: msangid@purdue.edu (M.D. Sangid).

https://doi.org/10.1016/j.compstruct.2018.08.029
Received 20 January 2018; Received in revised form 30 June 2018; Accepted 14 August 2018
Available online 17 August 2018
0263-8223/

simple to more complex cross-sections. However, this procedure requires the continuous adaptation of structuring elements which can be very intractable for highly dense fibrous network with tortuous architecture.

Several researchers have developed methodologies that involve a series of techniques to artificially decrease the diameters of fibers (thinning) thereby generating skeletal structures, which preserve the important topological features of the fibrous architecture. This is followed by the separation or merging of these skeletonized configurations at branch points given the prescribed constraints [25–30]. Despite several modifications and extensive use, thinning frameworks provide no indication of how many distinct fibers are contained within conjoined volumes of closely clustered fibers. Thus, these frameworks are often restricted to low volume fraction fibrous systems where the strands are composed of simple cross-sections [24].

Germain and Martin-Herrero [31] proposed a *heavy ball* method that separates the edges of touching fibers by first using successive 2D morphological operations (erosions and dilations) and thereafter uses the trajectory of a ball (whose size is adaptable to the diameter of each hole) to separate individual fibers within the sub-volume. Though this framework ensures the preservation of the distinct fiber diameters, the utilization of 2D splitting techniques to generate the hole-mouths is limited to the in-plane information of the features and this could be misleading, therefore unsuitable for complex cases.

Furthermore, although there exist commercial tools with exhaustive image processing and visualization facility for characterizing fibrous systems, they do not offer enough flexibility to mitigate 3D fiber reconstruction anomalies. Additionally, they lack a platform to interact with tracking algorithms necessary to compute the evolution of the reconstructed individual fibers.

From the aforementioned discussions it is noted that: (i) reconstruction results generated from frameworks that rely directly on the fiber intensity maps may be compromised when applied to noisy image volumes, (ii) the generation of the 3D sub-volume microstructure based solely on the direct application of robust 2D morphological operations on the serial sections of 3D image volume is not reliable for rendering intricate microstructure, and (iii) most purely 3D approaches are based on fiber skeletonization/thinning frameworks which are mostly restricted to low volume fraction fibrous systems composed of simple cross-sections [24]. Taking cognizance of the abstractions from the aforementioned discussions, and in contribution to the on-going efforts aimed at probing fibrous systems, this study proposes a novel synergistic framework (robust 2D segmentation and 3D reconstruction approaches), where matching segmented features on successive slices of a 3D image volume are stacked up to generate a crude 3D architecture which is further refined by utilizing 3D information. The proposed framework aligns itself more to methods that trace fibers following the center of mass of their constituent ellipses [32]. Though these methods have a limitation when it comes to tracing of fibers with complex cross-sections [24], especially in cases of high volume fractions of fibers, the proposed framework addresses this limitation by incorporating multiple reference frame analysis through supervised iterations to ensure the faithful reconstruction of the fibrous sub-volume architecture. Ultimately, this synergistic framework not only mitigates the limitations of a purely 2D mathematical morphology approach while rendering an accurate microstructure (with a much lower complexity than what is usually adopted in a purely 3D approach), but also is capable of efficiently reconstructing and characterizing discontinuous composites with a high volume fraction (which possess engineering significance due to increased mechanical strength).

The implication of the current approach provides a new paradigm in composite damage analysis. The current state of the art in damage mechanics homogenizes damage by primarily linking the deterioration of the tensors of the elastic modulus to the accumulated damage [33–35]. Approaches aimed at estimating effective properties in composites using orientation distribution functions [10,36,37] are in no doubt suitable candidates to determine states of homogenized damage in composites. This framework, on the other hand introduces an explicit implementation of sub-volume microstructural features (individual fibers) to track damage events, such as fiber breakage and fiber pull-out.

The following sections of this paper are described as follows; Section 2 discusses the material used and the non-destructive technique modality adopted in this work: tomography and the generation of 3D image volumes represented as 2D slices (tomograms). Section 3 discusses the 2D segmentation approach; a four-step sequential framework adopted for segmenting the features on the generated tomograms. Section 4 discusses the proposed 3D fiber reconstruction algorithm with an incorporated multiple reference frame analysis to ensure the faithful rendering of the 3D fiber structures. Section 5 discusses the results from the algorithm, highlighting the potential benefits from the proposed framework.

2. Materials and tomographic reconstruction

In this study, a cylindrical tensile specimen machined from injection molded rods is analyzed. The specimen is composed of discontinuous glass fiber polypropylene matrix composite provided by DuPont. Aside from the sufficient phase contrast that a glass fiber filler in a polypropylene matrix provides, the excellent innate properties of glass fibers [38–40] and polypropylene polymer [41,42] makes it a utility composite for diverse applications [3], thus leading to its choice as a case study for this research.

Fig. 1 illustrates the 3D volume representation of the gage section, after the tomography studies were conducted. Tomography is a non-destructive imaging technique used to visualize the internal features of an object without any interference from over/underlying structures. The use of X-rays is one of the commonly associated imaging modality in tomography, where measurements of the attenuation of X-rays incident to a specimen on a rotating stage are extracted as a series of projection images (sinograms). These sinograms are then converted to a

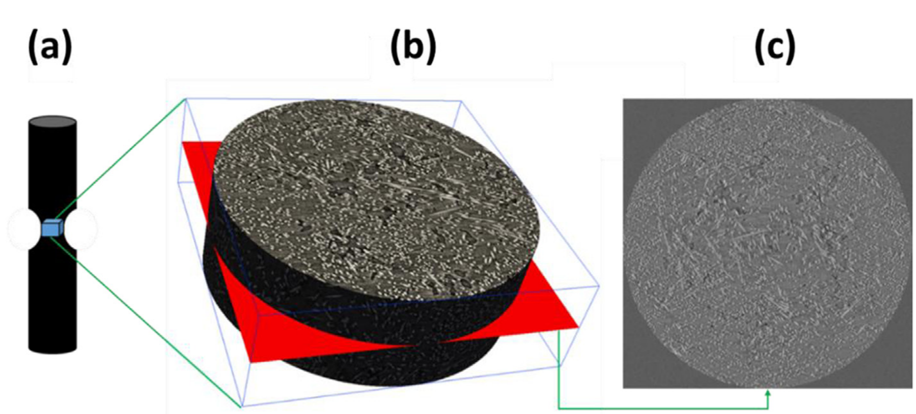

Fig. 1.. 3D image volume representation of the gauge section: (a) Sample specimen with highlighted gauge section of diameter of 2.42 mm; (b) 3D volume micrograph after tomographic reconstruction of sinograms; (c) Slice representation of 3D micrograph insert highlighted in red. (For interpretation of the references to colour in this figure legend, the reader is referred to the web version of this article.)

3D image volume of the specimen (Fig. 1b) represented as series of grayscale images (Fig. 1c) using an appropriate tomographic reconstruction algorithm [43,44]. The minimally invasive nature of X-ray tomography allows for quantitative measurements to be made on resulting digital images for sub-volume characterization.

For this study, X-ray tomography was carried out at the 2-BM beamline at the Advanced Photon Source (APS) at Argonne National Laboratory where a monochromator was used to emit 25 keV X-rays to the cylindrical specimen, which was placed 75 mm from the detector. The specimen was rotated through 180° in 0.12° incremental steps per projection for a total of 1500 projections. The exposure time per projection was 100 ms at a scan rate of 0.5°/s. Projection images, recorded by a lens-coupled CCD camera at 5x magnification with a pixel size of 1.3 µm, were then converted to a series of grayscale images using Tomopy [45], a gridded reconstruction algorithm for real-time tomography [46,47].

3. Four-step sequential 2D segmentation approach

Segmentation is an important prerequisite for most types of image analysis [48–50]. However, images are fraught with random fluctuation of pixel values (noise), introduced during image generation and acquisition. Fig. 2a is a serial section of the greyscale tomogram where the dark greyscale intensity regions represent defects such as voids and microcracks. Since these features have well-defined edges, they can be captured using intensity based thresholding methods. The emphasis of the present study is on the segmentation and extraction of the fibers (e.g. high-intensity regions). This section, details a framework where, the high-intensity features are segmented and the in-plane geometric properties of ellipses that bound segmented features (metadata) are extracted using a four-step sequential framework which comprises: (i) image sharpening, (ii) watershed segmentation, (iii) watershed optimization, and (iv) post processing and extraction of the metadata of the optimized segmentation results.

3.1. Iterative utilization of the unsharp masking technique (2D framework Step 1)

Generally, the effect of blur on tomograms is random and sometimes localized. There is, therefore, the need to progressively mitigate the effects of the blur; specifically, in this research, a piece-wise approach is taken. To achieve this, different brightness level versions (the number of which is dependent on how blurry the edges of the features are) of an original tomogram are created and respectively subjected to the unsharp masking technique [51–53].

After enhancing the contrast on the different brightness level versions of the original tomogram, each version is further preprocessed to indicate locations of regional minima (locations of the catchment basins during implementation of watershed segmentation) on the image. The preprocessing begins with binarization (the classification of the features into foreground, i.e. features of interest, and background regions) using the Otsu method [54,55]. A negative distance transform of the image's compliment is then generated from the binarized image which is used to create a mask (another binary image) where all areas in the distance

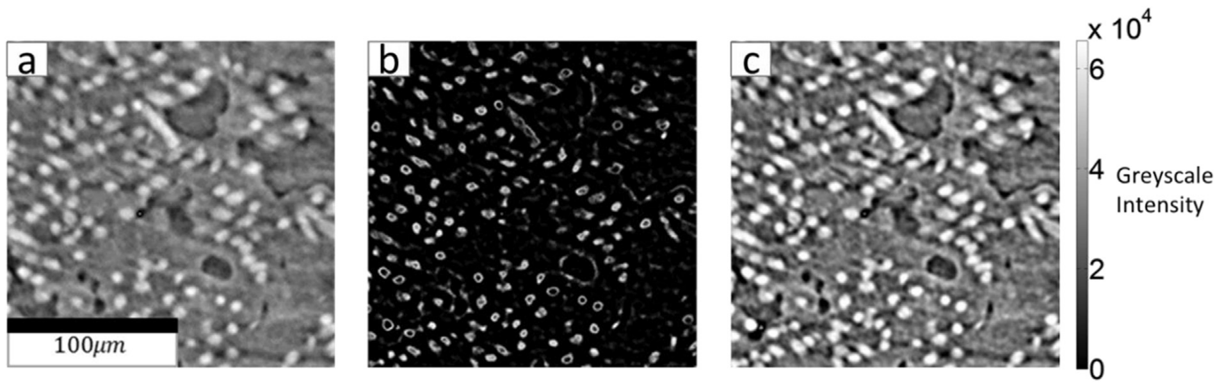

Fig. 2. Description of the unsharp masking technique: (a) The original tomogram prior to sharpening. (b) The unsharp mask which is generated by subtracting a blurred version from the original image. (c) Overlaying the mask over the original image and enhancing the contrast around the features gives an overall sharper image.

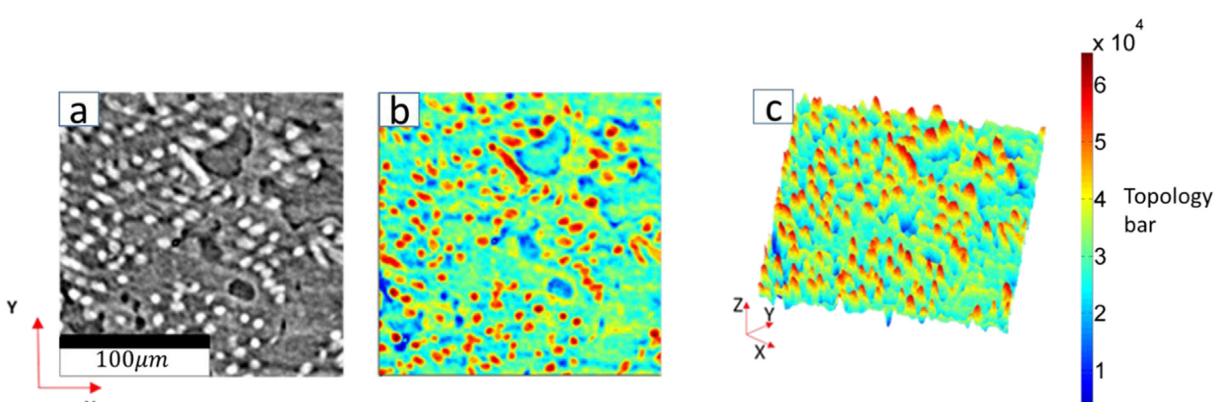

Fig. 3. Topological representation of (a) a grayscale image. (b) The red regions refer to the high- intensity/bright pixel areas in (a) which are represented as the crests in (c). The darker regions in (a) are represented as the troughs in (c). (For interpretation of the references to colour in this figure legend, the reader is referred to the web version of this article.)

transform with the change in intensity less than a certain threshold have a value of zero. Thereafter the pixel intensities of the grayscale tomogram are modified such that regional minima occur in locations with nonzero values indicated on the mask.

3.2. Iterative utilization of marker-controlled watershed segmentation (2D framework Step 2)

The features on the preprocessed images are segmented using the watershed transform, an image segmentation algorithm which transforms image's features (corresponding to heights and troughs (Fig. 3)) into well-defined pools (catchment basins) separated from each other by watershed ridge lines [56–60]. During watershed segmentation there is the need to incorporate a control mechanism to address under- or over-segmentation. To achieve this, markers are set within the catchment basins to indicate the size of segmented regions (marker-controlled watershed segmentation [59,60]). For optimum segmentation, it is encouraged to adopt an iterative utilization of user-defined markers based on some a priori information of feature sizes (Algorithm 1). For instance, in this research, matrix burn-offs and the microscopy of similar specimens revealed fiber distributions of ~10 µm diameters with a standard deviation of about 2 µm. Thus, iterative segmentation of a feature is deemed satisfactory if the minor axis length of an ellipse (which can be proved to be the diameter of the fiber) that circumscribes that feature is well within a prescribed threshold which considers the reported statistics of the fiber diameter distribution.

Algorithm 1.Pseudo code of the Iterative watershed segmentation.

Declare the variables f_b, f_t and m_t as described in code

Variable	Description
f_b	mean fiber diameter
f_t	threshold for the ellipses with minor axis lengths slightly above f_b and snuggly fit around segmented regions
m_t	vector of marker sizes to provide check against over- and under-segmentation

(*Phase* 1)

Binarize grayscale, GS_{image}, using Otsu Method
Compute a negative of the distance transform to generate a mask , D
Impose regional minima on GS_{image} using mask D and first entry of marker value $m_t(1)$
Apply watershed segmentation, $Watershed_{Function}$
Extract Stats (the properties of ellipses circumscribing segmented regions)

initial watershed procedure

(*Phase* 2)

if (some segmented features have minor axis lengths greater than prescribed f_b)
  classify such regions as poorly segmented regions and extract their respective indices as idx_{bad}

  for (*each member in* $m_t(h)$*, where h ranges from second to last element*)

    GS_{image} = update GS_{image}, keeping only pixel intensities of poorly segmented features, using idx_{bad}
    Repeat steps in initial watershed procedure with GS_{image} and $m_t(h)$

  % extract all the minor axis lengths
    $m_v = [Stats.MinorAxisLength];$

  % find seperate indices based on threshold, f_b
    $idx_{invalid} = find(m_v > f_b)$
    $idx_{valid} = find(m_v \leq f_b)$

  % extract snuggly fit ellipses with indices slightly above f_b
    $idx_{temp} = \left(idx_{invalid} \mid idx_{invalid}\left(\frac{Pixel\ of\ region}{Area\ of\ bounding\ ellipse}\right) \geq f_t\right)$
    $idx_{final} = sort\left([idx_{valid} \cup idx_{temp}], 'ascend'\right)$

  % keep ellipses that satisfy f_b with marker value $m_t(h)$
    $[Stats\_iter\_keep\{t\}] = Stats(idx_{valid});$
    $idx_{bad} = idx_{valid}\left(\sim ismember\left(idx_{valid}, idx_{temp}\right)\right)$
  end

end
  % Concatenate metadata of ellipses satisfying f_b after applying watershed segmentation over the range, m_t
  Stats = (Stats ∪ Stats_iter_keep{t}});

3.3. Optimizing of watershed segmentation results through piecewise mitigation of blur (2D framework Step 3) and extraction of metadata of optimized segmentation results (Step 4)

To ensure that the watershed segmentation results is not biased due to the image's brightness level, the best case-by-case comparison of corresponding segmented regions of respective sharpened versions of an image is considered. Fig. 4 illustrates the watershed segmentation results of two brightness level versions of a tomogram (after each, their respective features were enhanced using the unsharp masking technique). Analyzing corresponding regions reveals cases of under-segmentation (A), region sensitivity to fringes due to blur (D) and uncaptured regions due to brightness levels (B and C). This classification is based on; (i) size of competing ellipses (smaller areas are much preferred since they are insensitive to fringes due to blur), (ii) the spatial location of centroids and (iii) the degree of area overlap between competing ellipses (to ensure that regions of only significant overlaps are compared).

Suppose $\{k, \theta_k, C_k, M_k, m_k, A_k\}$ and $\{\widehat{p}, \widehat{\theta_p}, \widehat{C_p}, \widehat{M_p}, \widehat{m_p}, \widehat{A_p}\}$ are metadata of brightness level versions 1 and 2 respectively, where for instance, $\{k, \theta_k, C_k, M_k, m_k, A_k\}$ are defined such that for each ellipse e_k in brightness level version 1: θ_k is the vector of pixel locations; C_k is the centroid co-ordinates; $M_k$is the major axis length; m_k is the minor axis length and A_k is the area. Furthermore, given that β and $\widehat{\beta}$ are binary images composed of elliptical regions (generated from the metadata $\{k, \theta_k, C_k, M_k, m_k, A_k\}$ and $\{\widehat{p}, \widehat{\theta_p}, \widehat{C_p}, \widehat{M_p}, \widehat{m_p}, \widehat{A_p}\}$, respectively), then the notation $\beta(\theta_k)$ are the labels of ellipses in $\beta$with pixel locations defined by θ_k. When the binary image β is overlaid unto the binary image $\widehat{\beta}$, then for a given ellipse e_k in β, the variable $\widehat{i_p}$ corresponds to labels of ellipses in $\widehat{\beta}$ that overlap the ellipse e_k in β and this can be expressed in Eq. (1) as:

$$\widehat{i_p} = \{unique(\widehat{\beta}(\theta_k) \neq 0)\} \tag{1}$$

After the extraction of$\widehat{i_p}$, the difference between the area of ellipse e_k and the areas of its corresponding ellipses in $\widehat{\beta}$ associated with labels in $\widehat{i_p}$ is then computed as expressed in Eq. (2) as

$$A_v = \{\widehat{A}(\widehat{i_{p,j}}) - A_k\}, \ \forall\, j = 1 \cdots .length(\widehat{i_p}) \tag{2}$$

where, $length(\widehat{i_p})$ refers to the cardinality (number of elements) of the vector $\widehat{i_p}$; and $\widehat{A}(\widehat{i_{p,j}})$ refers to the *jth* component of a vector of ellipses' labels in $\widehat{\beta}$ that overlap e_k when $\widehat{\beta}$ is superimposed on β. To ensure sensitivity to fringes due to blur when comparing overlapping regions in β and $\widehat{\beta}$, the condition in Eq. (3) must be enforced.

$$all\{A_v\} \geq 0 \quad \& \quad \frac{\sum \widehat{A}(\widehat{i_p})}{A_k} \geq a_t, \tag{3}$$

where a_t, is the threshold to curb the response to fringes. The first part of the condition in Eq. (3) stipulates that all competing ellipses must be smaller in area and the second part of the condition restricts this decrease to an allowable threshold. The logic behind this condition is that, though smaller areas are most likely indicative of segmentation results insensitive to blurry fringes, the piecewise mitigation of blur between β and $\widehat{\beta}$, necessitates the change in area between the overlapping segmented regions to be gradual (no abrupt area changes). Following the satisfaction of the condition in Eq. (3), overlapping regions are further probed to ensure that only sufficiently overlapping ellipses are compared. These checks include a confluence (percentage overlap) check, given by Eq. (4a) and Eq. (4b) and a spatial location of competing ellipses' centroids check, given by Eq. (5).

$$\widetilde{\theta}(j) = \frac{\widehat{\theta_{p,j}} \cap \theta_k}{\widehat{\theta_{p,j}}} \ such\ that\ \widehat{\beta}(\widehat{\theta_{p,j}}) = \widehat{i_{p,j}}, \quad \forall \quad j = 1 \cdots length(\widehat{i_p}) \tag{4a}$$

$\widetilde{\theta}$ in Eq. (4a) refers to the ratio of the intersection of pixel locations between overlapping ellipses $\widehat{e_p}$ and those of the ellipse e_k to the pixel locations between overlapping ellipses. Indices of the overlapping ellipses in $\widehat{i_p}$ with associated θ greater than a certain threshold, c_t, say 0.90 confluence, are extracted as $\widehat{i_{m*}}$ as expressed in Eq. (4b).

$$\widehat{i_{m*}} = \{\widehat{i_{m,j}}\}, \quad where \ (j|\widetilde{\theta}(j) > c_t), \quad \forall \quad j = 1 \cdots length(\widehat{i_m}) \tag{4b}$$

The centroids of the overlapping ellipses with indices defined in the vector $\widehat{i_{m*}}$ are then subjected to a spatial location of competing ellipses' centroids check expressed as Eq. (5).

$$||\widehat{C_m}(\widehat{i_{m*}}), C_k|| \leqslant 0.5{*}M_k \tag{5}$$

where $||\cdot||$ represents the Euclidean distance between centroids of the overlapping ellipses with indices defined in the vector $\widehat{i_{m*}}$ and the centroid of the ellipse e_k. In Eq. (5), the acceptable centroid deviation of centroids of overlapping ellipses ·. is constrained such that it cannot be more than half the major axis length of the ellipse e_k.

The implementation of case-by-case comparison of segmentation results ensures an accurate segmentation of serial sections of highly clustered out-of-plane fibers. However, segmentation of the in-plane fibers is very challenging since the serial sections of the in-plane fibers have more surface area and thus are susceptible to the effects of radiographic streaks, making over-segmentation of in-plane features inevitable. To address this, a multiple reference frame analysis of in-plane fiber is implemented and the segmentation results of the serial sections perpendicular the plane, in which the in-plane fiber lies, is selected. This idea will be further explored in Section 4 of this paper. Finally, in order to fully capture features within the tomogram, segmented features whose boundaries touch the edges of the tomogram and their corresponding metadata are deleted. Fig. 5 is a schematic that summarizes the four-step sequential 2D characterization procedure.

4. 3D volume rendering algorithm

The volume rendering algorithm involves the stacking of the elliptical regions on the serial sections of the image volume obtained from the segmentation results of the sequential framework to generate a crude microstructure characterized by distinct or conjoined dendritic strands. The crude microstructure is further dissected through a sequential separating scheme to a more refined morphology that faithfully represents the microstructure. Before discussing the components of the 3D volume rendering algorithm (Fig. 7), two outstanding issues with regards to the in-plane fibers will be addressed: (i) it was noted in Section 3.3 that in-plane fibers were more susceptible to over-segmentation due to the effects of radiographic streaks and (ii) even if the effects of the streaks were to be mitigated, the crude 3D microstructure generated by stacking the elliptical regions of the in-plane fibers will be rendered as an ellipsoid instead of a cylinder. Consider an image volume sliced along the three mutual perpendicular axes (Fig. 6), where Fig. 6b represents serial sectioning along the loading axis and Fig. 6a and c represent serial sectioning along directions perpendicular to the loading axis. It can be observed that features that were in-plane fibers for serial sections along the loading direction will now become out-of-plane fibers for serial sections along perpendicular directions. Thus the segmentation results for serial sections of in-plane fibers along the loading axis are replaced by the segmentation results of the same fiber for serial sections along the other axis perpendicular to the previous axis. Utilizing this logic ensures that the inherent cylindrical 3D form of reconstructed fibers is always preserved. In other words, a multiple reference frame analysis compares independently generated 3D reconstruction results from serial sections along three mutually perpendicular axes. The 3D reconstructed result along the serial section that possesses the maximum number of constituent ellipses is the most accurate 3D reconstruction as segmentation along this direction has minimal interactions with noise and also ensures the cylindricity of the fiber.

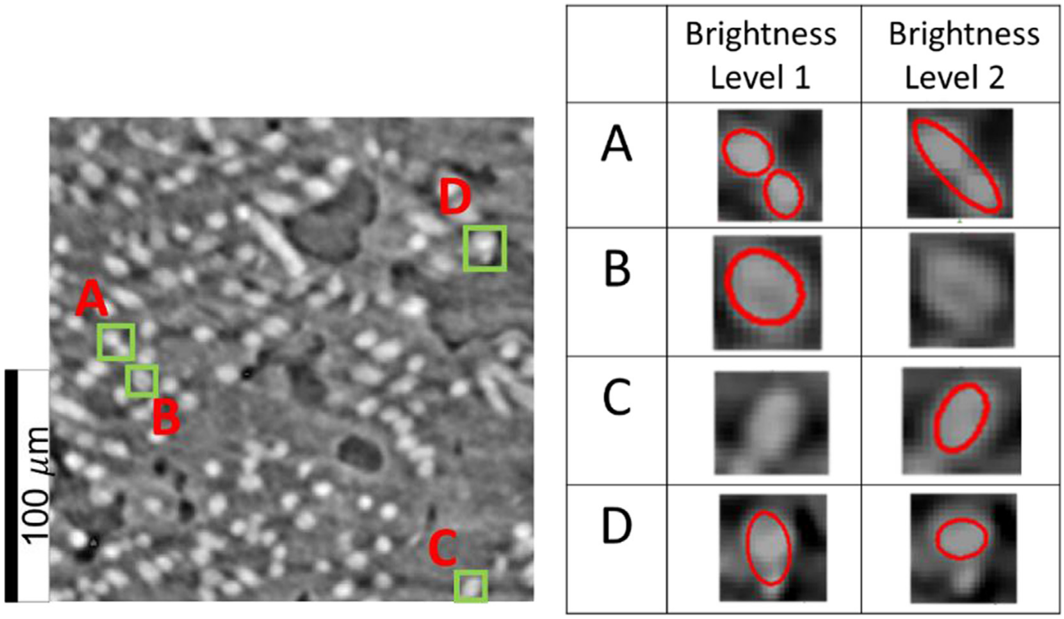

Fig. 4. Optimization of watershed segmentation through the comparison of watershed results of different contrast versions of the same image. (A) indicates regions of under-segmentation; (B and C) indicates uncaptured regions due to brightness level; and (D) indicates region sensitivity to fringes due to blur. The competing regions are compared against each other and the best result is selected as the optimized segmentation of the feature in the original tomogram located in that region.

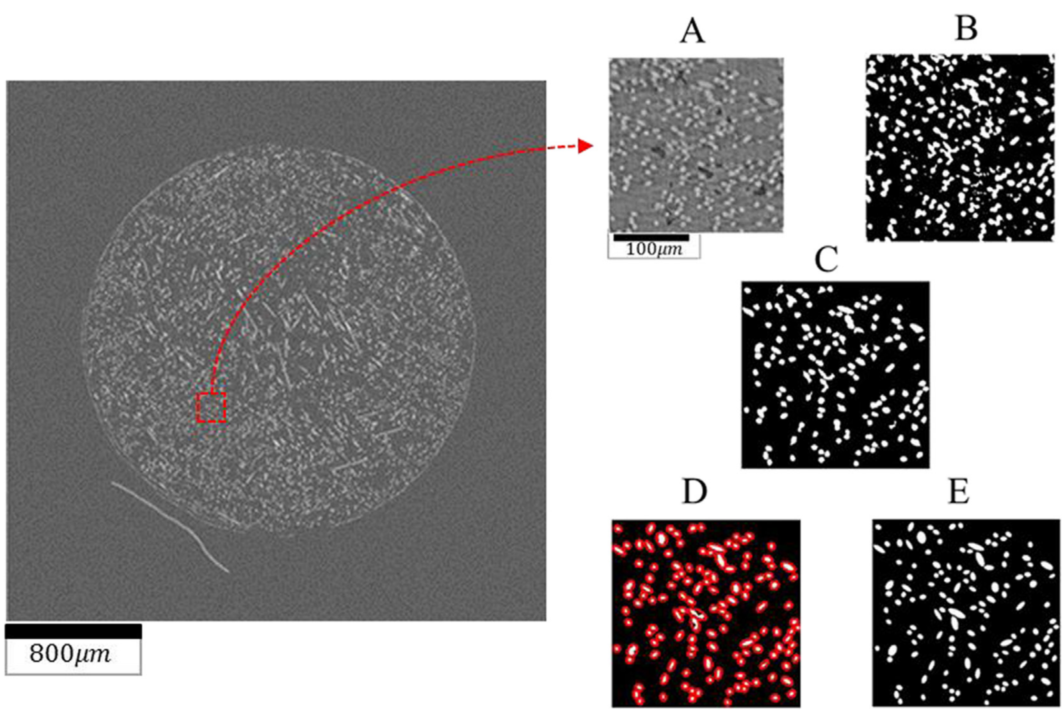

Fig. 5. Example of a reconstructed microtomography slice (left) and 2D characterization method for a small subset (right). Digital imaging techniques adopted by the code: (A) Cropped greyscale image; (B) Marker-controlled watershed segmentation; (C) Image after removing pixels below a threshold and at the boundaries; (D) Fitted ellipses around the amorphous regions; and (E) Replacement of segmented regions with the fitted ellipses and the creation of the in-plane geometry properties.

4.1. Generation of crude 3D fiber morphology (Stage 1)

Stage 1 of the volume rendering algorithm involves the stacking of elliptical regions on successive slices based on minimal centroid deviation (comparatively least in-plane) distance between any two ellipses on consecutive slices. The basis for this comparison is due to the fact that the distance between consecutive slices is 1 μm; therefore, the centroids of stacked ellipses for a fiber (herein referred to as candidate constituent ellipses) are not expected to vary significantly. A visual representation of the framework is summarized using Fig. 8. In this figure, it is observed that for clustered elliptical regions, when the radial neighborhood of an ellipse's centroid (seed ellipse) on the current slice (slice 1 in Fig. 8) is projected onto successive slice (slice 2 in Fig. 8), there are incidents of non-unique mapping, (a many-to-one mapping), indicated by the green and red dashed lines. By incorporating the condition of minimal centroid deviation, this non-unique mapping is resolved by selecting the pair with the least in-plane distance (Δ_1 as shown in Fig. 8b) which in this case is ellipse-pair A-C.

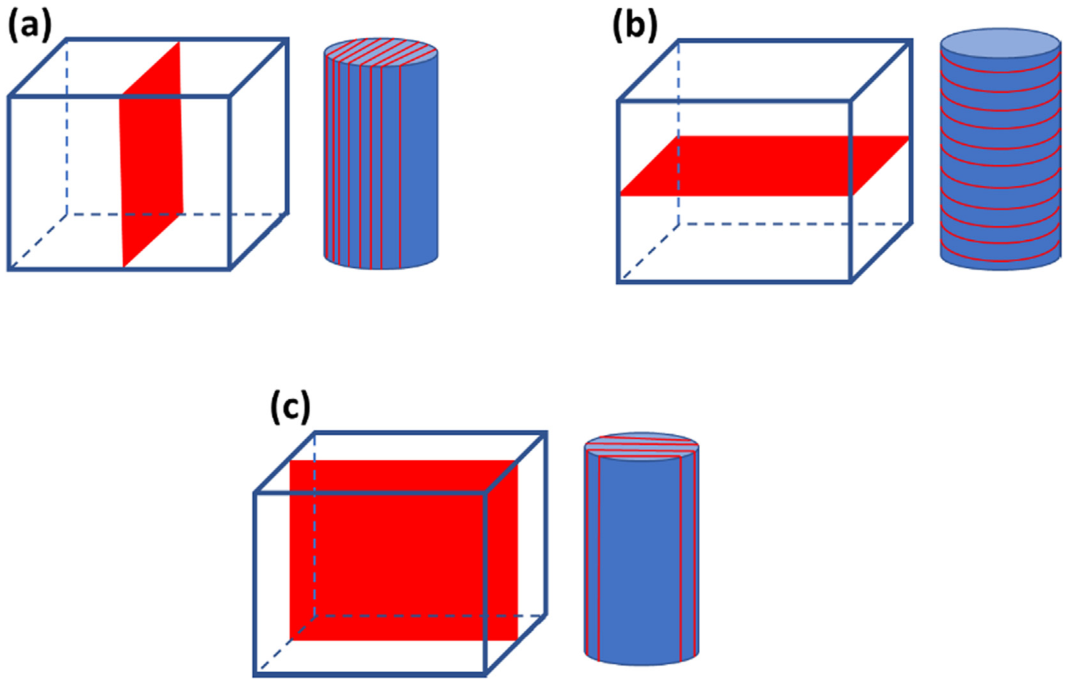

Fig. 6. Schematic of the 3D volume rendering algorithm. The red inserts in each of the cubes represent the respective slices on which the 2D segmentation is performed. Beside each cube is an illustration of the 3D reconstructed results. 3D rendering for cases (a) and (c) will be flattened ellipsoids, whilst the result in case (b) will preserve the 3D cylindrical form expected of the fiber. (For interpretation of the references to colour in this figure legend, the reader is referred to the web version of this article.)

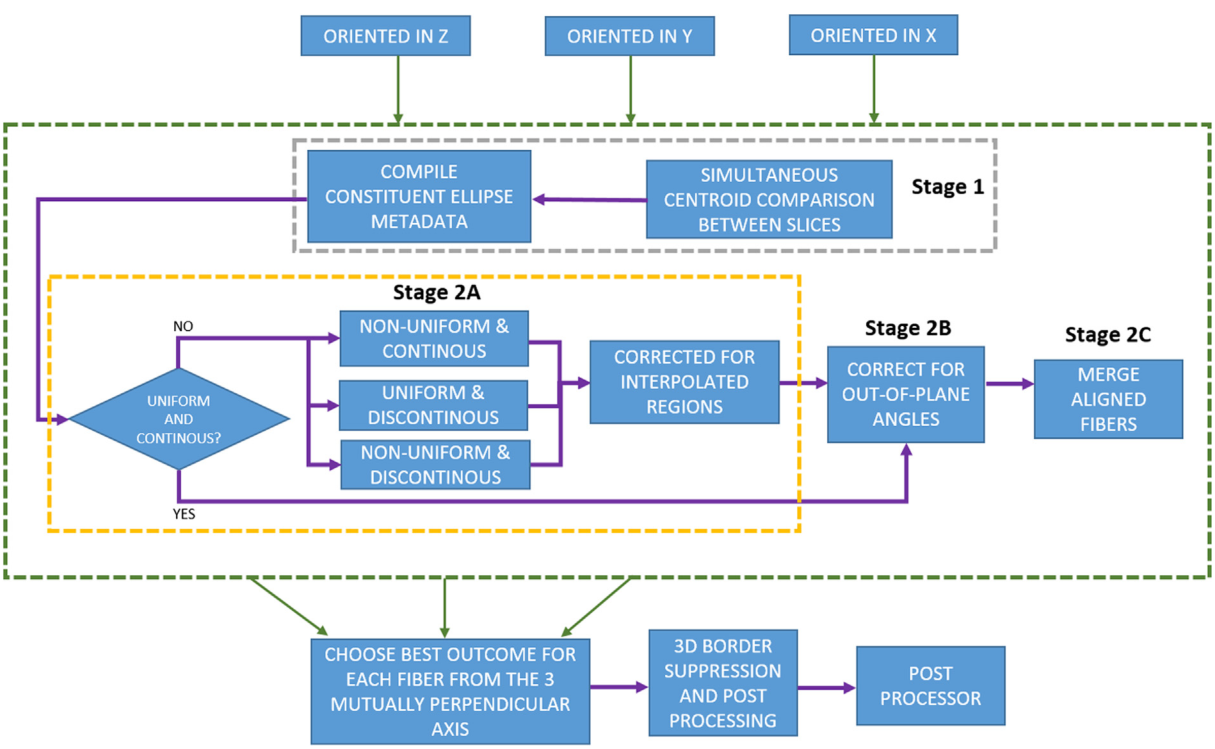

Fig. 7. Schematic of the 3D volume rendering algorithm. The algorithm slices the 3D image volume into a series of slices whose normal align with the x, y, and z directions. Thereafter the results of the respective segmentations are subjected through the Stages 1 and 2 of the volume rendering algorithm. Stage 1 of the algorithm generates a crude microstructure by stacking matching ellipses on successive slices. Stage 2 refines this crude microstructure by separating lumped fibers and stitching fibers segments that need stitching. The respective reconstructed fibers are compared against each other based on the result that preserves the cylindrical 3D form expected for each fiber. 3D Border feature suppression is performed to extract fibers that are fully captured with a cylindrical boundary. These extracted fibers are then post-processed by characterizing them based on fiber length and orientation distributions.

Thereafter the associated metadata (in-plane geometrical properties) of the candidate constituent ellipses are extracted.

The immediate result of the stacking of consecutive ellipses based on the minimal centroidal deviation is an initial approximation of the microstructure characterized by crude fiber morphology, which for the most part could be categorized into non-uniform and continuous, uniform and continuous and non-uniform and discontinuous, as illustrated in Fig. 9. It should be noted that the discontinuous configurations refer to physically disjoint fibers which is a direct consequence of stacking elliptical regions based on minimal centroid variation with no threshold imposed on the minimal centroid variation. Consequently, preliminary reconstruction results such as the those in Fig. 9 (b, c) illustrating disconnects are likely to occur. The interpretation to these disconnects are that between the slices embedding the disconnected ellipses, there are no ellipses within a prescribed neighborhood that are comparatively best matches based on the minimal centroid variation except the disconnected ellipses. This case is easily resolved by imposing a threshold to disconnect such fibers. In this study, a Euclidean distance of $10\mu m$ was selected.

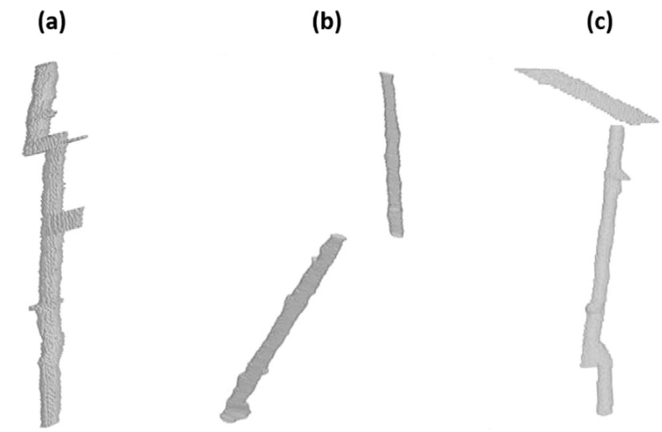

Fig. 9. Illustration of crude 3D fiber reconstruction after Stage 1 categorized as (a) Non-uniform and continuous, (b) Uniform and discontinuous, (c) Non-uniform and discontinuous.

4.2. Fiber separating algorithm (Stage 2A)

The sub-micron resolution of tomography may result in tomograms with highly indiscernible transitions between edges of clustered fibers. This situation, though sparingly occurring, is random and may be amenable by increasing the number of finer contrast thresholds (refer to Section 3.1) thereby increasing the computation time. A limited number of finer contrast thresholds, on the other hand, do prove effective for most of the fibers, however for the cases of the clustered fibers, they will be observed to be conjoined at certain locations. To address this scenario, a fiber separating algorithm framework was designed (Stage 2A). It works on the principle of locating these conjoined regions and splitting them into their appropriate sections using an alignment procedure illustrated in Fig. 10.

The fiber separation algorithm extracts the centroid locations of all the constituent ellipses of the fiber, and sets as outliers, regions with areas greater than one standard deviation away from the mean. This procedure extracts regions A, B and C as illustrated in the Fig. 10 (illustrated in Step 1). The causes of these anomalous regions are majorly bifold; anomalous regions resulting from the edge effects of the blur that persists through a considerable depth (illustrated by regions A and B in Step 1) and anomalous regions resulting from the conjoined fibers (illustrated by region C in Step 1). 3D skeletonized forms of the 3D fiber illustrated by the blue dashed line shows off-set centroids (illustrated by the blue dotted line in Step 2) due to these anomalous regions. To resolve this, the fiber separating algorithm performs an alignment of centroids of ellipses bounding the regions A, B and C. For cases of reasonable alignment, the centroids within the bounding ellipses are replaced by the interpolation values obtained by linear interpolation between the sandwiched constituent ellipses. As in the case of region B, this operation corrects for the offset centroids caused by its anomalous size (illustrated by the black dotted line in Step 4). For cases of misalignment, the region between the bounding ellipses is split by linearly projecting through the volume with the centroid position of the bounding ellipses (illustrated by the green and red dotted lines in Step 4). The algorithm radially populates around the neighborhood of the segmented centroids to a sufficient diameter proportional to the mean of the constituent centroids of the reconstructed fiber and threshes out the fringes.

4.3. Out of plane angle correction (Stage 2B)

Glass fibers are generally brittle in nature [61–63]. Therefore, it is necessary to constrain the 3D tortuosity of all reconstructed fibers to prevent cases of highly misaligned or kinked 3D reconstructed fiber [64], as illustrated in Fig. 11a. This is implemented by first using singular value decomposition (SVD) [65,66] to perform 3D orthogonal distance regression linear fit, in a progressive manner along the length of the fiber. To increase the accuracy of the 3D line fits, outlier points for each n-successive centroid are removed using Cook's distance prior to the implementation of the 3D linear fits. Cook's distance for a set of points shows the influence of each observation on the fitted response,

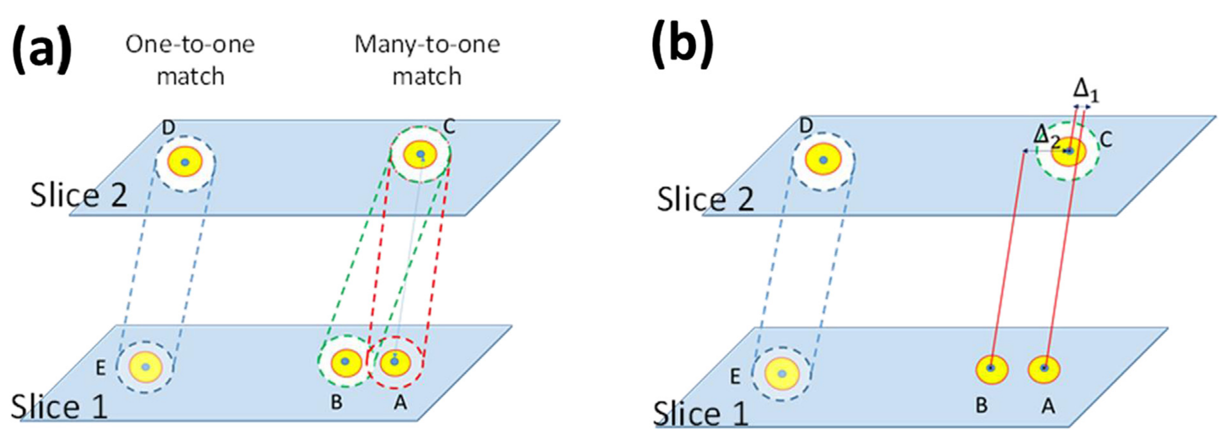

Fig. 8. Stacking elliptical regions based on minimal centroid variation. The candidate constituent ellipses E and D illustrate the non-ambiguity associated with matching candidate consecutive ellipses for regions sparsely populated fibers. For regions of clustered populated fibers ellipses, A, B and C illustrate the associated ambiguity. Fig. 8b shows the result of how the bifold comparison addresses this ambiguity.

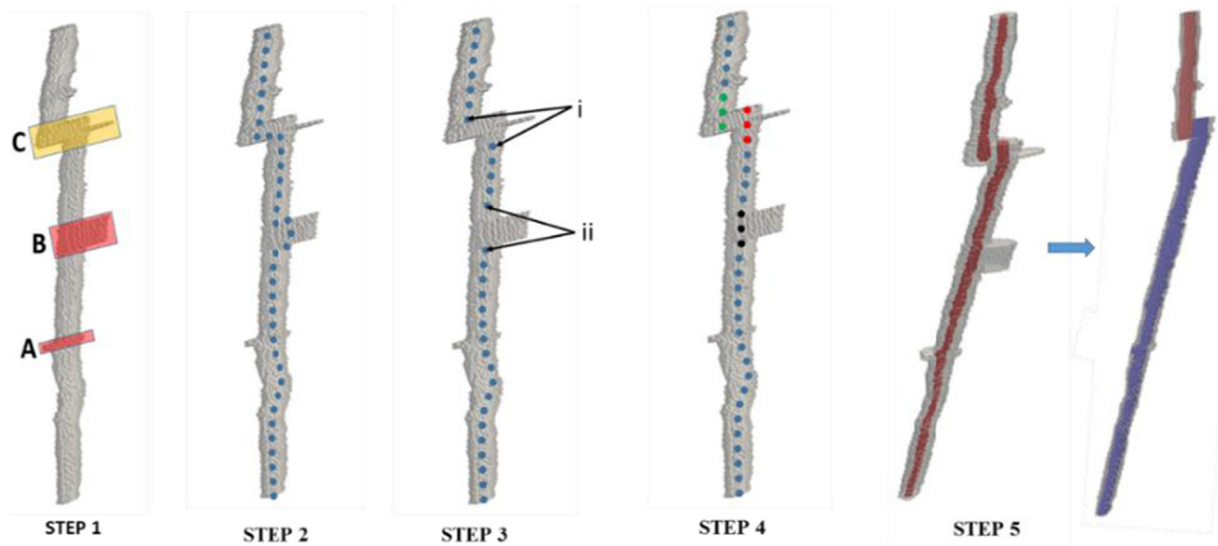

Fig. 10. Illustration of fiber separating algorithm. In this figure, step 1 refers to the detection of anomalous areas. These areas arise due to edge effects around the features (highlighted in red rectangle) or poor segmentation of clustered fibers (highlighted in the yellow rectangle). Step 2 refers to a 3D skeletonized view of the constituent ellipses. Steps 3 and 4 isolates the ellipses of the anomalous areas and refits the interpolated centroids using the alignment of the centroid of ellipses that bound the anomalous regions. Step 5 radially grows the fibers to a sufficient diameter and further threshes out the fringes due to the blur. (For interpretation of the references to colour in this figure legend, the reader is referred to the web version of this article.)

i.e. the nature of the regression model created with and without a particular observation [67,68]. In this research, the adopted method for potential outliers were centroids whose associated Cook's distances that are greater than one standard deviation from the mean of all the Cook distances. Thereafter the angles between the direction vectors from linear fits (from SVD) of the respective segments are evaluated using the inner product of the direction vectors. Using the evaluated angles, a condition is set such that for any two successive segments, if the angle evaluated is within acceptable levels according to a prescribed threshold, those segments are considered as constituent segments as expressed in Eq. (6).

$$arccosine(a{\cdot}b) \leq \theta_t \tag{6}$$

where, θ_t is the angular threshold limiting the 3D tortuosity. Fig. 11 is an illustration, where constraining the 3D tortuosity of a reconstructed fiber refines the morphology into two distinct fibers using Eq. (6).

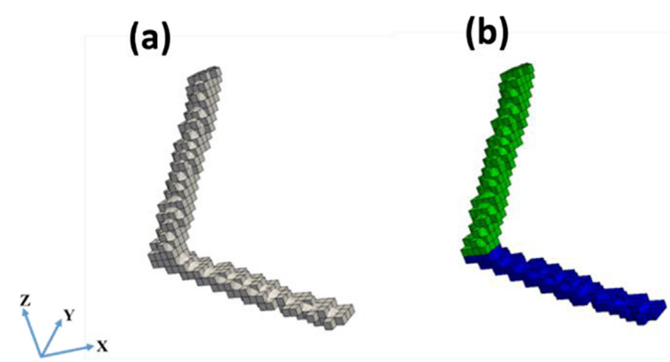

Fig. 11. Illustration of the 3D reconstructed fiber before and after the application progressive linear fits along the fiber using SVD and the constraint on the angle between associated direction vectors of the linear fits. (a) represents the bifurcated fiber prior to Stage 2B. (b) is the result obtained after the segmentation of the fiber at the bifurcated junction using 3D orthogonal distance regression linear fit in a progressive manner along the length of the fiber.

4.4. Further stitching of fibers

Due to the complex nature that clustered fibers pose for segmentation, the crude fiber morphology may be characterized by strands of dissimilar fibers conjoined at distinct sections has been already discussed and the necessary steps to mitigate this issue has been addressed by the fiber separating algorithm (Section 4.2). It is possible that after refining the fiber sections through Stages 2A to 2B, the neighboring fibers within the conjoined vicinity will have fiber segments that stack up on each other and have similar orientation descriptions as illustrated in Fig. 12b. Thus Stage 2C isolates fiber segments that stack onto each other with similar orientation and stitches them as one fiber (illustrated in Fig. 12c).

After the Stage 2C, the multiple reference frame analysis (discussed in Section 4) is implemented and the most accurate fiber reconstruction is chosen. Thereafter, a 3D border suppression step, where reconstructed fibers whose boundaries touch the bounds of a cylindrical shell (to mimic the geometry of the gage-section) are deleted to avoid erroneous sub-volume feature characterization, especially for determination of the fiber length.

The data format for an image volume is a 3D 16-bit unsigned integer array. The algorithm was implemented in MATLAB, and the final 3D array containing the labelled reconstructed fibers was converted to a hierarchical data format (hdf) file and viewed in Paraview (Fig. 13). With a desktop computer of an i7-4930 K CPU and 64 GB RAM, the runtime for the 4 stage segmentation of the 2D slices of a sub-volume of 355 μm by 355 μm by 354 μm is ~1.2 h, and for a much larger dataset, of dimensions 1399 μm by 1399 μm by 750 μm, as shown represented in Fig. 13, the runtime is ~48 h. The runtimes for the 3D reconstruction of the same volumes are 0.75 and 7 h, respectively.

5. Discussion

5.1. Versatility of segmentation routine

The segmentation routine adopted in this research involves a piecewise approach that accurately segments the features within the tomograms by mitigating the random effects of blur causing radiographic artifacts. To begin the four-step sequential framework is equipped with several utilities to sharpen the edges of images features. These utilities include the specification of (i) the size of the edge regions, (ii) how much further apart adjacent values need to be for them to be considered as an edge, and (iii) the degree of exaggeration between edge

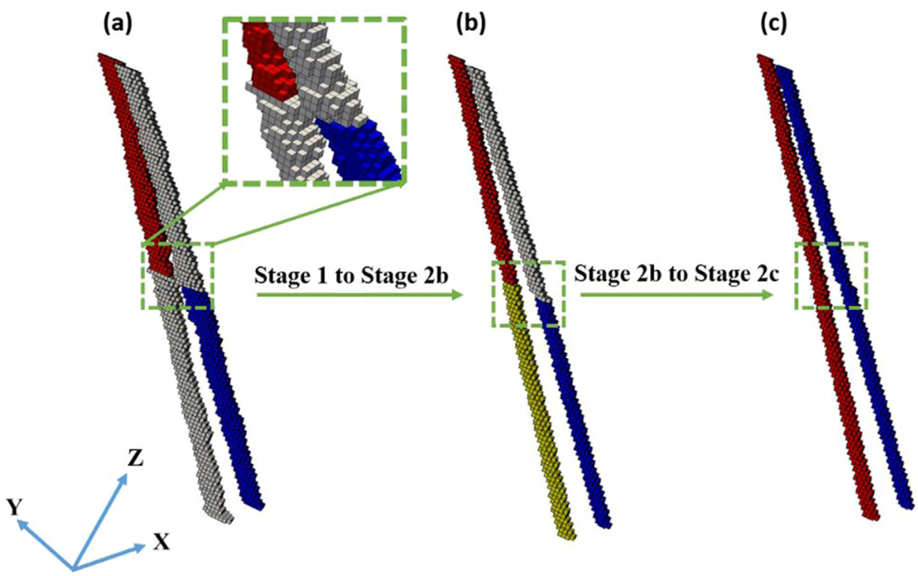

Fig. 12. Illustration of the result after applying Stage 2C. (a) Adjacent fiber with an insert that highlights an artifact due to fiber crossover. (b) An illustration of the result of the artifact observed in (a) after applying the fiber separation algorithm and the further segmentation constraining the 3D tortuosity of the segmented fibers. (c) The result after stitching neighboring fibers within the vicinity of the crossover, based on similar orientation descriptions.

differences. Additionally, the segmentation routine includes an in-built iterative implementation of a feature segmentation (based on training data) that takes into account the nuances between the respective sharpened versions of the original tomogram to generate reasonable segmentation results. Optimized feature segmentation is achieved by comparing the respective segmentation results of corresponding features against a suitable metric as discussed in Section 3.3. Ultimately, the proposed segmentation framework, when implemented affords the user more control on the effect that blurr has on feature segmentation, an attribute which is lacking in most commercial segmentation software [32] .

5.2. Comparison of reconstruction code to existing reconstruction frameworks

In this research, the synergistic approach of 2D segmentation with 3D techniques (discussed in Section 4 and 5) has been shown to be effective in reconstructing high volume fraction fibrous systems that consist of fiber with straight or gently curved morphologies and even to the more complex cases of conjoined regions due to fiber cross-overs. The framework is insensitive to the effects of noise that may compromise techniques relying directly on the fiber intensity maps on grey level image volumes to perform 3D fiber reconstruction [21,22]. Additionally, the framework (a confluence of 2D morphological techniques and 3D techniques) ensures high fidelity especially compared to techniques such as the heavy-ball approach [31], which may be problematic when adopted in highly clustered fibers forming an agglomerate with indiscernible edges (due to tomographic artifacts). Furthermore, unlike thinning algorithms [25–30], this framework not only provides some indication of how many fibers are present in a conjoined volume (by considering the number of ellipses and alignment of their respective centroids bounding the conjoined volumes), but also is applicable to highly dense sub-volume architecture. The incorporation of an intelligent multiple reference frame analysis (discussed in Section 4), resolves the reconstruction of the in-plane fibers, which are crucial features from the mechanistic stand point since these fibers carry no load and are probable sites for cracks to initiate.

5.3. Discussion of post-processed results

With complex morphologies resolved, morphological descriptors unique to each fiber such as the fiber length, diameter, orientation, volume fraction and the degree of cluster between fibers to mention but a few, can be conveniently computed. In this section, emphasis will be given to the fiber volume fraction, fiber length and orientation distributions measurements of the sub-volume architecture of the test specimen. The estimated fiber volume fraction of the 3D reconstructed fibers is 0.15, as compared to the value reported by the manufacturer of 0.16. The spatial orientation description of a fiber, on the other hand will be expressed as components of the so-called A_{ij} tensor [69].

$$A_{ij} = \begin{bmatrix} \sin^2\theta\cos^2\phi & \sin^2\theta\cos\phi\sin\phi & \sin\theta\cos\theta\cos\phi \\ \sin^2\theta\cos\phi\sin\phi & \sin^2\theta\sin^2\phi & \sin\theta\cos\theta\sin\phi \\ \sin\theta\cos\theta\cos\phi & \sin\theta\cos\theta\sin\phi & \cos^2\theta \end{bmatrix} \tag{7}$$

In this research, the Eulerian angles (θ and ϕ illustrated in Fig. 14a) unique to the fibers are extracted and using Eq. (7), the average values of the A_{ij} tensor for the reconstructed volume are reported as follows.

$$A_{ij} = \begin{bmatrix} 0.1362 & 0.0326 & -0.0088 \\ 0.0326 & 0.2854 & 0.147 \\ -0.0088 & 0.147 & 0.5784 \end{bmatrix} \tag{8}$$

The A_{33} component of the A_{ij} tensor depicts how well aligned the fibers are to the longitudinal axis of the cylindrical gauge section. From the diagonal of the A_{ij} tensor, the higher value of the A_{33} component indicates a preferred alignment towards the longitudinal axis of the gauge section. This is consistent with the fact that the gauge section of the specimens were machined down to the center of the injection molded rods, where fibers are expected to be well aligned.

Finally, Fig. 14b is a fiber length distribution of the fibers within the gauge of the tensile specimen. The distribution ranging from 2.6 μm to 1035 μm has a mean fiber length of ~126.3 μm and a mode value of 25 μm. The range of the detected fiber length statistics demonstrates the proposed framework's capability of detecting fiber lengths at minute length scales, well above the threshold for noise (2.6 μm), which are incapable to detect with conventional destructive methods such as microscopy.

6. Conclusion

In this paper, a framework for reconstructing the microstructure of short fiber reinforced composites has been discussed and the results illustrated. As a case study, tomograms from an injection molded cylindrical specimen composed of discontinuous glass fiber within a polypropylene matrix were analyzed. The proposed 2D/3D synergistic framework necessitated from the inherent limitation in the use of 2D characterization techniques to reconstruct complex microstructure as

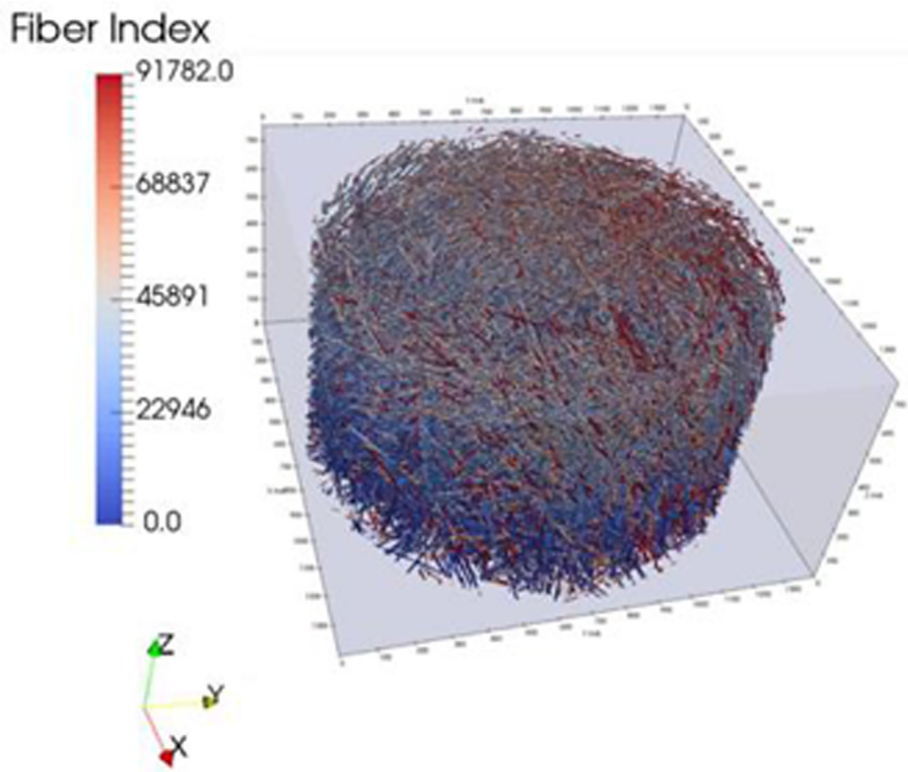

Fig. 13. Illustration of the result after 3D border suppression. In this figure, a 3D cylindrical subvolume is imposed on the reconstructed results such that fibers that are not fully captured within the boundary are thrashed out.

well as the mathematically intractable approach a purely 3D method requires. The 2D part of the framework comprised the use of the iterative utilization of the unsharp masking technique on the tomograms followed by the iterative marker-controlled watershed segmentation, denoising of segmentation results, fitting of ellipses around amorphous segmented results and the extraction of the in-plane geometry of elliptical regions. The 3D consideration of the framework stacks the elliptical regions on successive slices to create a crude 3D rendered microstructure (characterized by distinct dendritic strands of fibers). These are further dissected through a separating scheme to a more refined morphology. Further segmentation due to the constraint of the 3D tortuosity of the reconstructed fibers is performed using progressive linear fits along the fibers using SVD and the constraining the angle between the associated direction vectors.

To ensure that the cylindrical 3D reconstructed fibers are always preserved, a multiple reference frame analysis of each fiber is implemented and the segmentation results of the serial sections perpendicular to the plane in which the fiber lies is selected. 3D border suppression is then enforced on the optimized 3D reconstruction of the sub-volume to preclude all fibers that are not fully captured within a 3D cylindrical boundary. At this stage, the sub-volume architecture of the fibers can be characterized by means of fiber length and orientation distribution and the mean free path between neighboring fibers. In summary, this paper proposes a novel methodology to faithfully reconstruct the complex sub-volume architecture of the fibrous systems, thereby providing an accurate microstructure characterization. Additionally, this tool can be applied to 3D tomograms of successive loading configurations to track the evolution of the microstructure in order to gain insights on the underpinning physics of deformation of SFRCs.

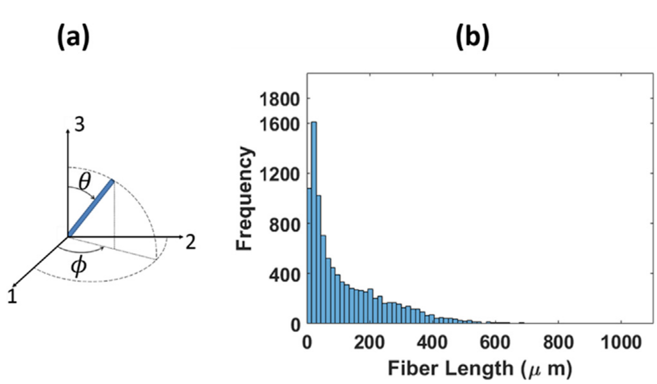

Fig. 14. (a) The description of fiber in terms of the Eulerian angles and (b) the fiber length distribution.

Acknowledgements

The authors gratefully acknowledge support from DARPA, Award No. HR0011-17-2-0069 and the National Science Foundation CMMI MoM, Award No. 1662554. The use of the Advance Photon Source (APS) is granted by the US Department of Energy, Office of Science, and Office of Basic Energy Sciences under Contract No. DE-AC02 06CH11357. The authors would like to thank Dr. Xianghui Xiao of the APS for assistance with data collection, Dr. Alan Wedgewood of Dupont for providing the material, and Mr. Imad Hanhan & Dr. Bhisham Sharma for many insightful discussions.

Appendix A. Supplementary data

Supplementary data associated with this article can be found, in the online version, at https://doi.org/10.1016/j.compstruct.2018.08.029.

References

[1] Mallick PK. Fiber reinforced composites: materials, manufacturing and design. CRC Press; 2007.

[2] Fu S-Y, Lauke B, Mäder E, Yue C-Y, Hu X. Tensile properties of short-glass-fiber- and short-carbon-fiber-reinforced polypropylene composites. Compos Part A Appl Sci Manuf 2000;31:1117–25. https://doi.org/10.1016/S1359-835X(00)00068-3.
[3] Karian HG. Handbook of polypropylene and polypropylene composites, revised and expanded CRC Press; 2003. https://doi.org/10.1201/9780203911808.
[4] Rosato DV, Rosato M. Injection molding handbook. Springer Science & Business Media; 2012.
[5] Plastic Bryce D. Injection molding manufacturing process fundamentals. Soc Manuf Eng 2001;1.
[6] Joffre T, Miettinen A, Wernersson ELG, Isaksson P, Gamstedt EK. Effects of defects on the tensile strength of short-fibre composite materials. Mech Mater 2014;75:125–34. https://doi.org/10.1016/j.mechmat.2014.04.003.
[7] Anlas G, Santare MH. A model for matrix cracking in short fiber composites. Int J Solids Struct 1993;30:1701–13. https://doi.org/10.1016/0020-7683(93)90199-H.
[8] Vaxman A, Narkis M, Siegmann A, Kenig S. Void formation in short fiber thermoplastic composites. Polym Compos 1989;10:449–53. https://doi.org/10.1002/pc.750100609.
[9] Fu SY, Lauke B. Effects of fiber length and fiber orientation distributions on the tensile strength of short-fiber-reinforced polymers. Compos Sci Technol 1996;56:1179–90. https://doi.org/10.1016/S0266-3538(96)00072-3.
[10] Fu S-Y, Lauke B. The elastic modulus of misaligned short-fiber-reinforced polymers. Compos Sci Technol 1998;58:389–400. https://doi.org/10.1016/S0266-3538(97)00129-2.
[11] Nguyen BBN, Bapanapalli SK, Phelps JH, Tucker III CL. Predictive engineering tools for fiber thermoplastic composites predictive engineering tools for injection-molded long-carbon-fiber thermoplastic composites. J Compos Mater 2014;42:1–43. https://doi.org/10.1177/0021998308088606.
[12] Clarke AR, Archenhold G, Davidson NC. A novel technique for determining the 3D spatial distribution of glass fibres in polymer composites. Compos Sci Technol 1995;55:75–91. https://doi.org/10.1016/0266-3538(95)00087-9.
[13] Davidson NC, Clarke AR, Archenhold G. Large-area, high-resolution image analysis of composite materials. J Microsci 1997;185:233–42. https://doi.org/10.1046/j.1365-2818.1997.1560712.x.
[14] Lee Y, Lee S, Youn J, Chung K, Kang T. Characterization of fiber orientation in short fiber reinforced composites with an image processing technique. Mater Res Innov 2002;6:65–72. https://doi.org/10.1007/s10019-002-0180-8.
[15] Agyei RF, Sharma B, Sangid M. Investigating sub-surface microstructure in fiber reinforced polymer composites via X-ray tomography characterization. 57th AIAA/ASCE/AHS/ASC Struct Struct Dyn Mater Conf 2016. p. 1–6. https://doi.org/10.2514/6.2016-0409.
[16] Jolly M, Prabhakar A, Sturzu B, Hollstein K, Singh R, Thomas S, et al. Review of Non-destructive Testing (NDT) techniques and their applicability to thick walled composites. Procedia CIRP 2015;38:129–36. https://doi.org/10.1016/j.procir.2015.07.043.
[17] Milner TE, Goodman DM, Tanenbaum BS, Nelson JS. Depth profiling of laser-heated chromophores in biological tissues by pulsed photothermal radiometry. J Opt Soc Am A Opt Image Sci Vis 1995;12:1479–88. https://doi.org/10.1364/JOSAA.12.001479.
[18] Chapman D, Thomlinson W, Johnston RE, Washburn D, Pisano E, Gmür N, et al. Diffraction enhanced X-ray imaging. Phys Med Biol 2015;42(1997):2025. https://doi.org/10.1088/0031-9155/42/11/001.
[19] Dolatowski ZJ, Stadnik J, Stasiak D. Applications of ultrasound in food technology. ACTA Sci Pol 2007;63:89–99.
[20] Adams RD, Cawley P. A review of defect types and nondestructive testing techniques for composites and bonded joints. NDT Int 1988;21:208–22. https://doi.org/10.1016/0308-9126(88)90333-1.
[21] Eberhardt CN, Clarke AR. Automated reconstruction of curvilinear fibres from 3D datasets acquired by X-ray microtomography. J Microsc 2002;206:41–53. https://doi.org/10.1046/j.1365-2818.2002.01009.x.
[22] Sandau K, Ohser J. The chord length transform and the segmentation of crossing fibres. J Microsc 2007;226:43–53. https://doi.org/10.1111/j.1365-2966.2007.01748.x.
[23] Legland D, Beaugrand J. Automated clustering of lignocellulosic fibres based on morphometric features and using clustering of variables. Ind Crops Prod 2013;45:253–61. https://doi.org/10.1016/j.indcrop.2012.12.021.
[24] Viguié J, Latil P, Orgéas L, Dumont PJJ, Rolland du Roscoat S, Bloch JF, et al. Finding fibres and their contacts within 3D images of disordered fibrous media. Compos Sci Technol 2013;89:202–10. https://doi.org/10.1016/j.compscitech.2013.09.023.
[25] Wang Q, Huang X, Zhou W, Li J. Three-dimensional reconstruction and morphologic characteristics of porous metal fiber sintered sheet. Mater Charact 2013;86:49–58. https://doi.org/10.1016/j.matchar.2013.09.009.
[26] Gaiselmann G, Manke I, Lehnert W, Schmidt V. Extraction of curved fibers form 3D data. Image Anal Stereol 2013;32:57. https://doi.org/10.5566/ias.v32.p57-63.
[27] Tsarouchas D, Markaki AE. Extraction of fibre network architecture by X-ray tomography and prediction of elastic properties using an affine analytical model. Acta Mater 2011;59:6989–7002. https://doi.org/10.1016/j.actamat.2011.07.051.
[28] Lux J, Delisée C, Thibault X. 3D Characterization of Wood Based Fibrous Materials: an Application. Image Anal Stereol 2006;25:25–35. https://doi.org/10.5566/ias.v25.p25-35.
[29] Tan JC, Elliott JA, Clyne TW. Analysis of tomography images of bonded fibre networks to measure distributions of fibre segment length and fibre orientation. Adv Eng Mater 2006;8:455–500. https://doi.org/10.1002/adem.200600033.
[30] Yang H, Lindquist W. Three-dimensional image analysis of fibrous materials. Proc SPIE 2000;4115:275–82.
[31] Martín-Herrero J, Germain C. Microstructure reconstruction of fibrous C/C composites from X-ray microtomography. Carbon N Y 2007;45:1242–53. https://doi.org/10.1016/j.carbon.2007.01.021.
[32] Iassonov P, Gebrenegus T, Tuller M. Segmentation of X-ray computed tomography images of porous materials: a crucial step for characterization and quantitative analysis of pore structures. Water Resour Res 2009;45:1–12. https://doi.org/10.1029/2009WR008087.
[33] Chaboche JL. Continuous damage mechanics - A tool to describe phenomena before crack initiation. Nucl Eng Des 1981;64:233–47. https://doi.org/10.1016/0029-5493(81)90007-8.
[34] Voyiadis GZ, Kattan PI. Advances in damage mechanics: metals and metal matrix composites with an introduction to fabric tensors. Amsetrdam, Netherlands: Elsevier; 2006.
[35] Kachanov LM. Introduction_to_Continuum_Damage_Mechanics 1990:135.
[36] Mishurova T, Rachmatulin N, Fontana P, Oesch T, Bruno G, Radi E, et al. Evaluation of the probability density of inhomogeneous fiber orientations by computed tomography and its application to the calculation of the effective properties of a fiber-reinforced composite. Int J Eng Sci 2018;122:14–29. https://doi.org/10.1016/j.ijengsci.2017.10.002.
[37] Lu Y, Liaw PK. Effects of particle orientation in silicon carbide particulate reinforced aluminum matrix composite extrusions on ultrasonic velocity measurement. J Compos Mater 1995;29:1096–116. https://doi.org/10.1177/002199839502900805.
[38] Callister W, Rethwisch D. Materials science and engineering: an introduction. vol. 94. 2007. doi:10.1016/0025-5416(87)90343-0.
[39] Fitzer E, Kleinholz R, Tiesler H, Stacey MH, De Bruyne R, Lefever I, et al. Fibers, 5. Synthetic Inorganic. Ullmann's. Encycl Ind Chem 2000. https://doi.org/10.1002/14356007.a11_001.pub2.
[40] Ilschner B, Lees JK, Dhingra AK, McCullough RL. Composite Materials. Ullmann's. Encycl. Ind. Chem., Weinheim, Germany: Wiley-VCH Verlag GmbH & Co. KGaA 2000:467–97. https://doi.org/10.1002/14356007.a07_369.
[41] Maddah HA. Polypropylene as a promising plastic: a review. Am J Polym Sci 2016;6:1–11. https://doi.org/10.5923/j.ajps.20160601.01.
[42] Shubhra QT, Alam A, Quaiyyum M. Mechanical properties of polypropylene composites. J Thermoplast Compos Mater 2013;26:362–91. https://doi.org/10.1177/0892705711428659.
[43] Herman GT. Fundamentals of computerized tomography London: Springer London; 2009. https://doi.org/10.1007/978-1-84628-723-7.
[44] Landis EN, Keane DT. X-ray microtomography. Mater Charact 2010;61:1305–16. https://doi.org/10.1016/j.matchar.2010.09.012.
[45] Gurrsoy D, De Carlo F, Xiao X, Jacobsen C. TomoPy: a framework for the analysis of synchrotron tomographic data. J Synchrotron Radiat 2014;21:1188–93. https://doi.org/10.1107/S1600577514013939.
[46] Dowd BA, Campbell GH, Marr RB, Nagarkar V, Tipnis S, Axe L, et al. Developments in synchrotron X-ray computed microtomography at the National Synchrotron Light Source. Dev X-Ray Tomogr II; Proc Meet 1999; Denver, CO:Bellingham, WA, Society of Photo-Optical Instrumen. doi:10.1117/12.363725.
[47] Baker DR, Mancini L, Polacci M, Higgins MD, Gualda GAR, Hill RJ, et al. Lithos An introduction to the application of X-ray microtomography to the three-dimensional study of igneous rocks. Lithos 2012;148:262–76. https://doi.org/10.1016/j.lithos.2012.06.008.
[48] Hall EL. Computer image processing and recognition. Academic Press; 1979.
[49] Gonzalez RCR, Woods RER. Digital image processing. 3rd ed. Prentice Hall; 2008.
[50] Russ J. The image processing handbook. 6th ed. CRC Press; 2011.
[51] Jain AK. Fundamentals of digital image processing. vol. 46. 1989. doi: 10.1016/0734-189X(89)90041-8.
[52] Pratt WK. Introduction to Digital Image Processing. 2014. doi:10.1016/B978-0-12-374457-9.00001-9.
[53] Murphy DB. Fundamentals of light microscopy and electronic imaging. Wiley-Blackwell; 2012.
[54] Otsu N. A threshold selection method from gray-level histograms. IEEE Trans Syst Man Cybern 1979;9:62–6. https://doi.org/10.1109/TSMC.1979.4310076.
[55] Chen Y, Chen DR, Li Y, Chen L. Otsu's thresholding method based on gray level-gradient two-dimensional histogram. In: CAR 2010 – 2010 2nd Int Asia Conf Informatics Control Autom Robot 2010;3:282–5. doi:10.1109/CAR.2010.5456687.
[56] Bertrand G. On Topological Watersheds. J Math Imaging Vis 2005;22:217–30. https://doi.org/10.1007/s10851-005-4891-5.
[57] Couprie M, Bertrand G, Psi L, Esiee G. Topological grayscale watershed transformation. SPIE Vis Geom VI Proc 2003;3168:136–46. https://doi.org/10.1117/12.292778.
[58] Serra J. Image analysis and mathematical morphology. New York: Academic Press; 1982.
[59] Gonzalez RC, Woods RE, Eddins SL. Digital Image processing using MATLAB. 2009. https://doi.org/10.1002/1521-3773(20010316)40:6<9823::AID-ANIE9823>3.3.CO;2-C.
[60] Parvati K, Rao BSP, Das MM. Image segmentation using gray-scale morphology and marker-controlled watershed transformation. Discret Dyn Nat Soc 2008;2008.. https://doi.org/10.1155/2008/384346.
[61] Thomason J, Jenkins P, Yang L. Glass fibre strength—A review with relation to composite recycling. Fibers 2016;4:18. https://doi.org/10.3390/fib4020018.
[62] McBride A, Turek S, Zaghi A, Burke K. Mechanical behavior of hybrid glass/steel fiber reinforced epoxy composites. Polymers (Basel) 2017;9:151. https://doi.org/10.3390/polym9040151.
[63] Lee S, Park J, Shin D, Yoon D. Interfacial properties of glass fiber/brittle-ductile dual-matrix composites using micromechanical techniques and acoustic emission. Polym Compos 1999;20:19–28. https://doi.org/10.1002/pc.10331.
[64] Bapanapalli S, Nguyen BN. Prediction of elastic properties for curved fiber polymer

composites. Polym Compos 2008;29:544–50. https://doi.org/10.1002/pc.20394.
[65] Klema V, Laub A. The singular value decomposition: Its computation and some applications. IEEE Trans Automat Contr 1980;25:164–76. https://doi.org/10.1109/TAC.1980.1102314.
[66] Shlens J, View M. Introduction I. A Tutorial on Principal Component. Analysis 2014.
[67] Cook RD. Detection of Influential Observation in Linear Regression. Technometrics 1977;19:15. https://doi.org/10.2307/1268249.
[68] Marzjarani M. Sample size and outliers leverage, and influential points, and cooks distance formula. Int. J. Arts Commerce 2015;4:83–6.
[69] Advani SG, Tucker CL. The use of tensors to describe and predict fiber orientation in short fiber composites. J Rheol (N Y) 1987;31:751–84. https://doi.org/10.1122/1.549945.